DOI: 10.15480/882.9350

Eighth International Symposium on Marine Propulsors
smp'24, Berlin, Germany, March 2024

CFD Simulation of Propeller-Induced Pressure Pulses in the Behind-Hull Condition of a Bulk Carrier

Emre Cilkaya[1], Heather Peng[1], Alireza Jahanbakhsh[1], Lorenzo Moro[1] , Mohammed Islam[2], Wei Qiu[1]

[1]Department of Ocean and Naval Architectural Engineering, Memorial University of Newfoundland,St. John's, Canada
[2]National Research Council of Canada (NRC), St. John's, Canada

ABSTRACT

This study focuses on the self-propulsion performance of a PANAMAX bulk carrier model equipped with a fixed-pitch propeller and rudder. An analysis of propeller-induced pressure pulses under non-cavitating condition using computational fluid dynamics (CFD) simulations was conducted. The propeller-hull interactions and the resulting propeller-induced pressure pulses were predicted. Numerical simulations were performed using the StarCCM+ software, using three turbulence models: SST k-ω, Realizable $k-\epsilon$ and Elliptic Blending Reynolds Stress Model (EB-RSM). It is concluded that the EB-RSM predicts pressure amplitudes much closer to the experimental data than the other turbulence models.

Keywords

URANS, model bulk carrier, non-cavitating propeller, propeller-induced pressure pulsations, experimental validation

1 INTRODUCTION

The propeller-hull interaction is a critical aspect in the performance analysis of marine vessels. Understanding the complex flow dynamics around the propeller and its interaction with the hull and rudder is essential for optimizing propulsion efficiency and minimizing energy losses. One of the key phenomena associated with propeller operation is the generation of pressure pulses that propagate along the body surface. These propeller-induced pressure pulses have significant implications for vessel performance, including hydrodynamic forces, noise generation, and structural integrity. Furthermore, the increasing concerns about environmental effects and the well-being of passengers and crew members are driving the demand for more precise predictions of pressure pulses.

Muye et al. (2020) conducted a study on the numerical prediction of cavitation and hull pressure pulses induced by a marine propeller in behind-hull conditions of a model-scale container vessel using RANS. They validated the pressure pulses for non-cavitating conditions against experimental data and concluded that the numerical predictions slightly overestimated the pressure pulses. In their subsequent work (Muye et al. 2021), they performed numerical simulations of pressure pulses generated by a cavitating marine propeller in behind-hull conditions at a model scale, utilizing both RANS and IDDES (Improved Delayed Detached Eddy Simulation) approaches. Their conclusion was that, for higher-order Blade Passing Frequencies (BPF), IDDES predicts higher levels compared to RANS. In another study by the same researchers (Muye et al. 2019), simulations for two high-skew model-scale propellers were conducted. They found that for non-cavitating cases, the $SSTk-\omega$ model yields accurate pressure pulse predictions compared to experiments.

Paik et al. (2013) presented simulations of cavitation flow and hull pressure fluctuations caused by a marine propeller operating behind a hull. These simulations employed the Reynolds-Averaged Navier-Stokes (RANS) approach using FLUENT and included the modeling of a full hull body submerged under the free surface. They used RSM (Reynolds Stress Model) to model turbulence and Schnerr & Sauer as a cavitation model. The cavitation patterns and hull pressure fluctuations predicted by these simulations were validated against experimental data, particularly in the Samsung Cavitation Tunnel (SCAT), demonstrating good agreement with the results.

Furthermore, Gaggero et al. (2017) studied numerical simulations of cavitation and hull pressure pulses generated by a marine propeller operating behind a ship hull in model scale. Their work involved the use of commercial software Star-CCM+ and open-source tool OpenFOAM, using a Reynolds-Averaged Navier-Stokes (RANS) approach. Their predictions, compared to experimental measurements, demonstrated good agreement in terms of cavitation patterns and pressure pulse levels at various blade passing frequencies, especially with a refined mesh. The study further highlighted the significant contributions of sheet cavitation and tip vortex cavitation to the observed pressure pulses.

This study is part of a project named Propeller Induced Noise and Vibration (PINOV) that was carried out at the NRC-OCRE (Coastal and River Engineering Research Centre of the National Research Council of Canada) to

predict the noise generated by a rotating propeller under non-cavitating atmospheric conditions. The test program includes background noise, resistance, self-propulsion, and bollard tests. The experimental data was provided by NRC (National Reearch Council Canada) and is partially avaliable online by NRC reports such as Pallard (2015).

The main focus of this paper is to present the validation studies for the numerical simulation of these tests using RANS-based Computational Fluid Dynamics (CFD). The numerical settings were arranged based on the intensive numerical simulations performed by Jin et al. (2023), presenting best practice meshing settings (B.P. Settings) for a similar ship model. Therefore, bare hull resistance, open water propeller characteristics, and self-propulsion tow force were validated against experimental data using these settings. Finally, pressure pulses in behind-hull conditions were predicted by comparing them using three RANS-based turbulence models with the experimental data.

2 NUMERICAL METHODS

The simulations were conducted using the URANS solver in StarCCM+. For free surface simulations, the High Resolution Interface Capturing (HRIC) VOF scheme was applied. First order implicit scheme was chosen for the temporal discretization and second order scheme was used for the spatial discretization. The ship's dynamic motion in heave and pitch directions is modeled using Dynamic Floating Body Interaction (DFBI) and is coupled with mesh motion for propeller rotation in self-propulsion simulations with detailed propeller modeling.

2.1 Turbulence Modeling

In eddy viscosity models, the Reynolds stresses (analogues to strain-rate tensor) are associated with the mean velocity gradients, the turbulent kinetic energy and the eddy viscosity as described in the equation below,

$$\mathbf{T} = \mu_t[\nabla\overline{\mathbf{U}} + (\nabla\overline{\mathbf{U}})^T] - \frac{2}{3}\rho k\mathbf{I} \qquad (1)$$

where μ_t indicates the eddy viscosity and k is turbulent kinetic energy which can be solved from the transport equations in the turbulence models, such as $k-\epsilon$ and $k-\omega$.

It has been indicated that two-equation models can produce sufficiently accurate predictions for most ship hydrodynamic applications (ITTC 2011). Thus, shear stress transport $SSTk-\omega$ model, which solves two additional transport equations for turbulent kinetic energy (k) and turbulent kinetic energy dissipation rate (ω), was chosen for turbulence modelling. It provides significant improvements for the flows with severe adverse pressure gradients by accurately predicting the location of flow separation in comparison with other popular two-equation turbulence models ($k-\epsilon$ and $k-\omega$) (Menter 1994).

In the present work, the effect of the turbulence models on the propeller-induced pressure fluctuations on the hull was examined by comparing two eddy viscosity models, the Realizable $k-\epsilon$ model and the $SSTk-\omega$ model, with the Elliptic Blending Reynolds Stress Model (EB-RSM).

3 NUMERICAL SIMULATIONS

Numerical simulations were conducted for bare-hull resistance, propeller open-water performance, and self-propulsion of a bulk carrier model using a detailed propeller modeling method with $SSTk-\omega$ turbulence modeling. Results are presented in Fig. 4, Fig. 8, and Fig. 10.

The computational domain setup was based on the optimized mesh settings from Jin et al. (2023). The best-practice meshing settings were validated by comparing the global force results from the numerical simulations with the experimental data. The error is defined as $E\%D = (D-S)\times 100/D$ with D as the experimental value.

Subsequently, the pressure pulses in the behind-hull condition from the simulations were validated against the experimental data.

3.1 Bare-hull resistance

A bulk carrier model was used for the numerical simulations in this study. The nominal particulars of the model in the fully loaded condition is given in Table 1. The bare hull geometry used for the simulations is presented in Fig. 1.

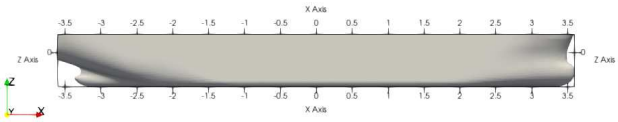

Figure 1: Model geometry of the bulk carrier

Table 1: Principle particulars of the model hull

Length, OA	7	m
Length, WL	6.9	m
Beam	1.25	m
Draft, Mean	0.46	m
Draft AP	0.46	m
Draft FP	0.46	m
Trim	0	m
Volume Disp	2.69	m^3
Displacement	2685.8	Kg

In this study, the location of the domain boundaries for the free surface simulations can be seen in Fig. 2. The inlet and outlet boundaries are $1.5L_{pp}$ and $3.0L_{pp}$ from the midship section, respectively. The side boundaries are $1.3L_{pp}$ from the centreplane. The bottom is $2.0L_{pp}$ below the free surface, and the top boundary is located $0.6L_{pp}$ above the free surface. Moreover, the origin of the cartesian coordinate system was located at the intersection point of the calm water surface, the midship section, and the ship's centreplane. The positive z direction points upward, and the positive x points from the stern to the bow.

The velocity boundary condition, i.e., a uniform incoming

flow was specified on the inlet. The pressure boundary condition was applied on the outlet boundary which is sufficiently far from the ship. Symmetric boundary conditions were set on two side boundaries to avoid flow reflected from the side boundaries. No-slip wall boundary condition was specified on the surface of the ship.

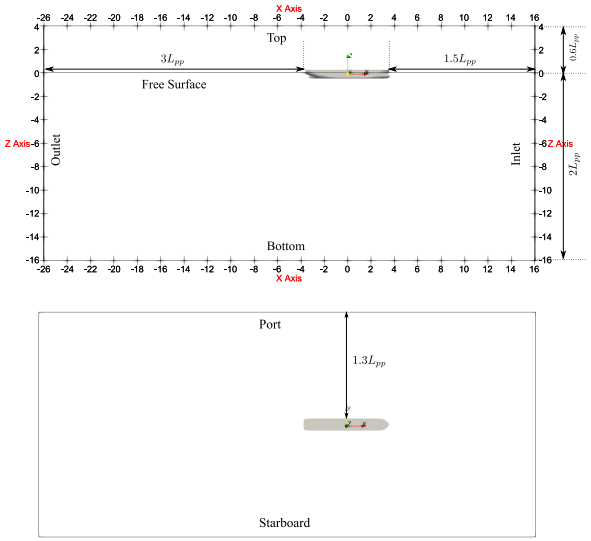

Figure 2: Computational domain for free surface simulations

In the context of marine hydrodynamics, accurately resolving the free surface between water and air is essential for capturing the free surface elevation and the wave-making component of ship resistance. When calculating the bare hull resistance of a ship, only the free surface and the wetted part of the hull surface are significant. Contributions from air resistance are negligible compared to the frictional and pressure resistance components of low speed ships such as bulk carriers. The hexahedral grid was constructed using the StarCCM+ trimmed mesher in order to have better quality prism layers along the hull. Figure 3 illustrates the meshes near the bow and stern, as well as the grids on the $z = 0$ m plane. The prism layer growth was intentionally stopped at the sharp edges near the skeg to prevent the numerical errors caused by mesh quality issues in this region. The number of cells generated for the bare-hull simulations was around 2.5 million. The numerical settings for the bare-hull simulations are summarized in the Table 2 in comparison with the best practice settings (B.P. Settings) from Jin et al. (2023). Here, $L_{pp}/\Delta x$ denotes number of cells per ship length.

Table 2: Numerical settings for Bare-hull simulations

Item	Variable	Settings	B.P. Settings
Mesh size	$L_{pp}/\Delta x$	552	518
	y^+	50	[50 - 125]
Time step	CFL	1.0	≤ 2
Turbulence model	$SSTk-\omega$		$SSTk-\omega$ & Realizable $k-\epsilon$

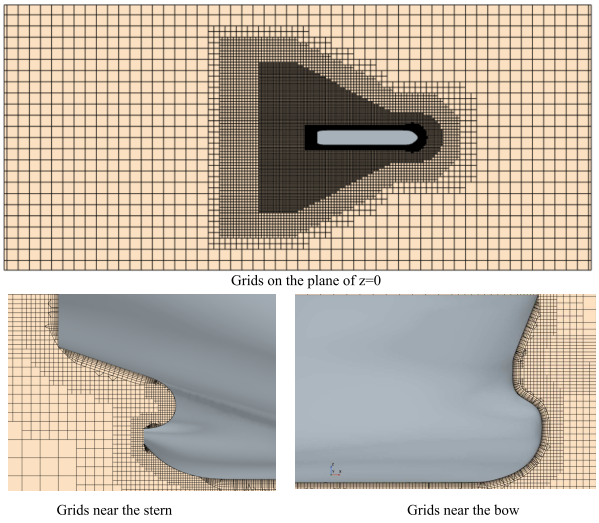

Figure 3: Mesh for bare hull resistance

The total resistance was predicted at five forward speeds corresponding to Froude numbers of 0.088, 0.111, 0.133, 0.155, and 0.178. The computational results were compared with the experimental results as shown in the Figure 4 and Table 3. It is observed that the numerical results agree well with the experimental data. The maximum relative error, found at $Fn = 0.088$, is 7.2%, while all other errors are below 3.0%.

Table 3: Relative errors for bare-hull simulations

Fn	R_T - Numerical (N)	R_T - Experimental (N)	|E% D|
0.088	13.774	12.847	7.213
0.111	20.470	19.904	2.842
0.133	27.987	28.678	2.410
0.155	36.960	37.861	2.381
0.178	52.070	52.617	1.040

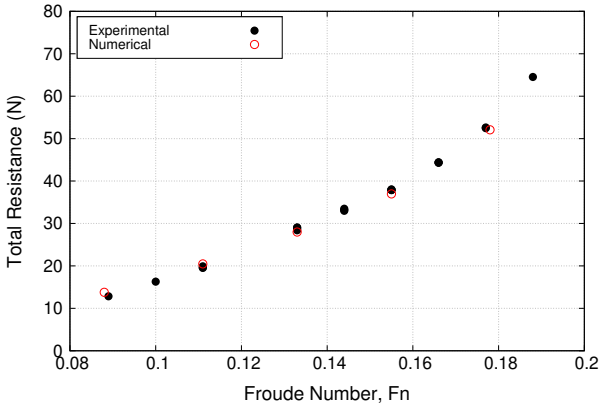

Figure 4: Total resistance curve in comparison with experimental data

3.2 Open-water simulation

The propeller geometry used in open water simulations is presented in Fig. 5 and Table 4 shows the principle particulars of the propeller.

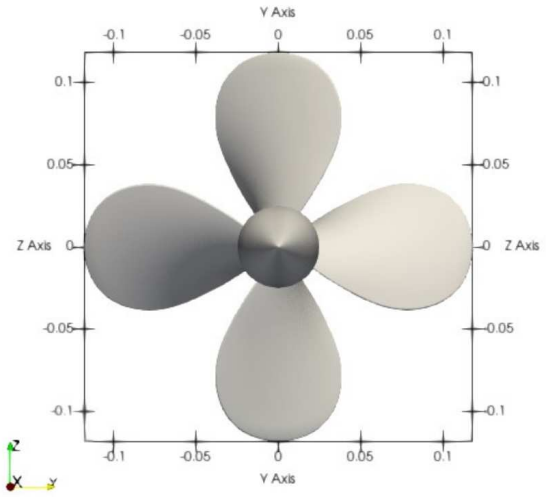

Figure 5: Model propeller geometry

Table 4: Principle Particulars of the Model Propeller

Parameters	Description
Diamater (m)	0.235
Number of Blades	4
Pitch-dimater (P/D) distrubution	Constant P/D=1.1
Expanded area ratio (EAR)	0.65
Section profile	NACA 66 modified with 0.8 meanline

The computational grids for the propeller open water simulations were also generated using the StarCCM+. The inlet boundary was placed $2.0D$ from the propeller center, the outlet boundary was set at $4.0D$ behind the propeller plane, and the diamater of the cylindrical computational domain was set $4.0D$. The computational domain includes two regions as stationary, and the rotating region as shown in Fig. 7. The number of cells generated for the open water simulations was around 11.9 million. The details of the mesh around the propeller blade is given in Fig. 6. The numerical settings for the open water propeller simulations are presented in Table 5. In the table below, the rotation rate of propeller, Tm, is denoted as m degrees per time step, and Δx/D is the non-dimensional body mesh size.

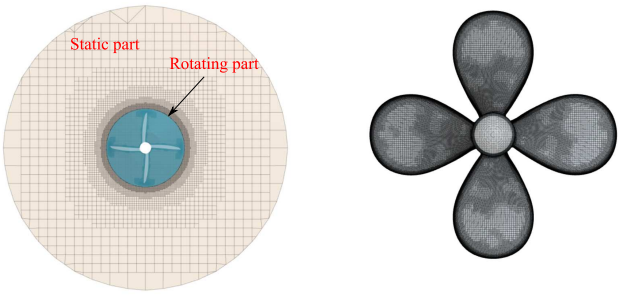

Meshes of static and rotating parts

Grids for the propeller model

Figure 6: Meshes for the propeller, the static part and the rotating part

Table 5: Numerical settings for open water simulations

Item	Variable	Settings	B.P. Settings
Mesh size	Δx/D	0.053	≤ 0.056
	y^+	47	[50 125]
Time step	Tm	$1^\circ/\Delta t$	$[1^\circ/\Delta t, 2^\circ/\Delta t]$
Turbulence model	$SSTk-\omega$		$SSTk-\omega$ & Realizable $k-\epsilon$

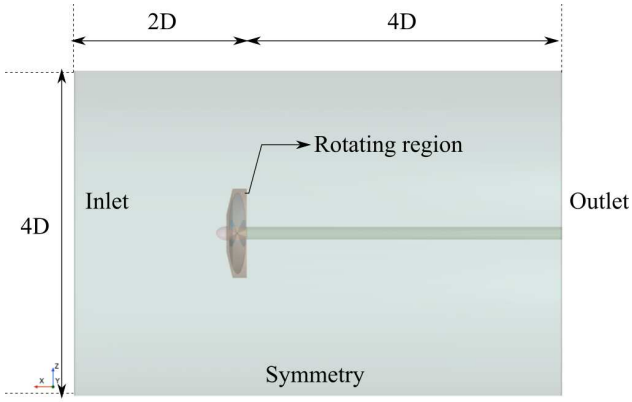

Figure 7: Computational domain for open water propeller simulations

The results, in comparison with the experimental data, are presented in terms of open water propeller force coefficients in Fig. 8. It can be seen in the figure that, at $J = 0.2$, the maximum error for Kt is 5.3%, with all other values falling below 5%. The relative errors for the force coefficients are tabulated in the Table 6.

Table 6: Relative errors for open water simulations

J	$K_t - \lvert E\%D\rvert$	$10K_Q - \lvert E\%D\rvert$	$\eta_0 - \lvert E\%D\rvert$
0.2	5.276	0.515	4.957
0.4	4.825	1.715	3.225
0.6	3.221	1.422	1.960
0.8	2.525	0.056	2.878
1	4.095	4.501	0.737

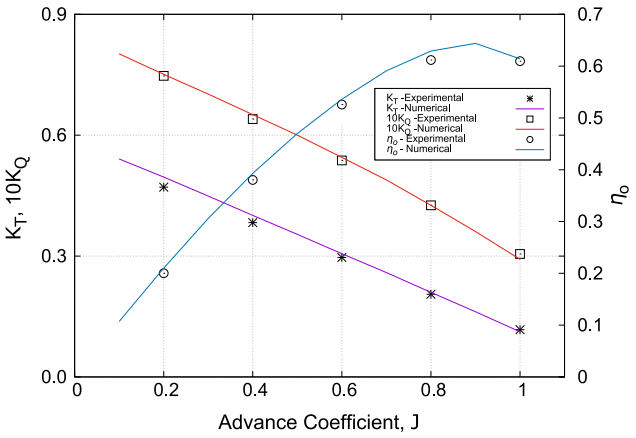

Figure 8: Open water propeller curve in comparison with the experimental data

3.3 Self-propulsion simulations

Self-propulsion of the bulk carrier model with the detailed propeller modelling method was simulated at the forward speed of $U = 1.376m/s$ for six propeller rotational speeds in order to determine model self propulsion point. The computational domain remains consistent with the description provided for the bare hull simulations earlier. The domain includes a rotating part with the propeller model and a static part everywhere else.

The mesh for the self-propulsion simulation with the detailed propeller method is presented in Fig. 9, where the rotating part is indicated in blue. The sliding mesh method was applied at the interface between the rotating and static parts. A y^+ value of around 45 was maintained for the propeller, while the hull's y^+ was set to approximately 50. The same non-dimensional mesh parameters were employed for the propeller region as well as for the hull.

To account for the presence of the propeller and capture its vortex, an additional refinement zone was implemented in the stern region of self-propulsion with detailed propeller modeling method. The number of cells generated for the self-propulsion simulations was around 8 million.

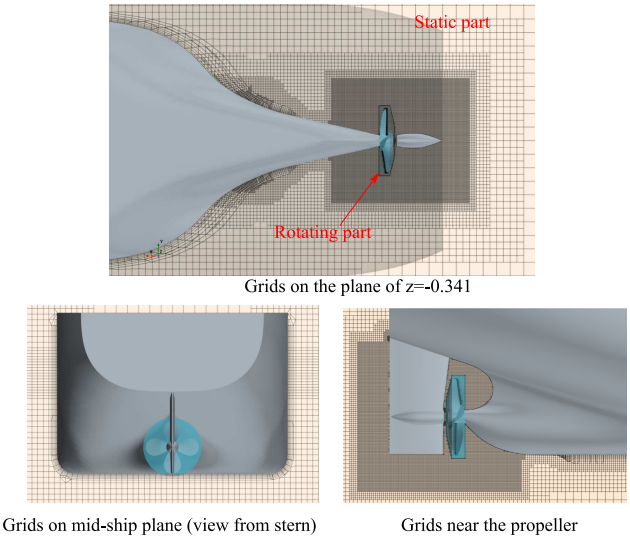

Figure 9: Mesh for self-propulsion simulations with detailed propeller modelling

The results are given in terms of the resultant force on the post F which is described as $F = R_T - T$, where R_T is the total resistance and T is the thrust generated by the propeller. The numerical results are summarized in the Table 7.

Table 7: Self propulsion simulation results using varying load method

Cases	n (rps)	F (N) - numerical
Case-1	6	19.449
Case-2	6.5	12.691
Case-3	7	5.163
Case-4	7.5	-2.832
Case-5	8	-12.595
Case-6	8.5	-19.949

Referring to the Fig. 10, the self-propulsion point is predicted to be $7.27rps$. When compared to the experimental self-propulsion point at $7rps$, this yields a relative error of 3.8%.

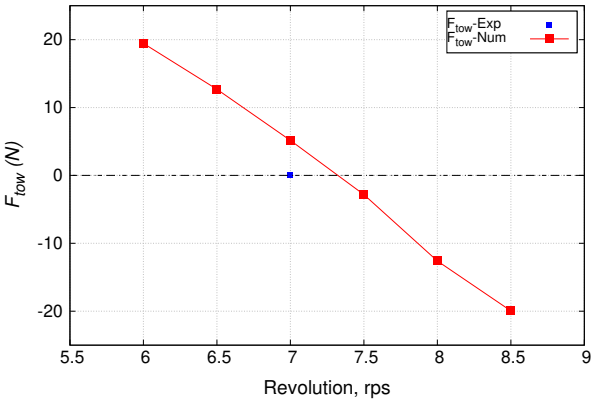

Figure 10: Tow force vs. rps graph

3.4 Pressure pulse predictions in behind-hull condition

After validating global force results against the experimental data for bare hull resistance, open-water propeller, and self-propulsion simulations, pressure pulses were recorded at 12 measurement probes on the hull above the propeller, as shown in Fig. 11, corresponding to the same measurement locations as in the model test.

The pressure amplitudes at each probe are presented in Fig. 11, compared with the experimental data for the bollard pull case at $n = 4.5$ rps using the $SSTk - \omega$ turbulence model. The maximum pressure amplitude is observed at probe 4, and the numerical pressure amplitudes generally agree well with the experimental data, although the pressure amplitude was underpredicted at probes 11 and 12 in comparison with the experimental data. Additionally, not much difference in pressure amplitudes was observed between the static simulations and the dynamic simulations, where trim and sinkage remain unrestricted.

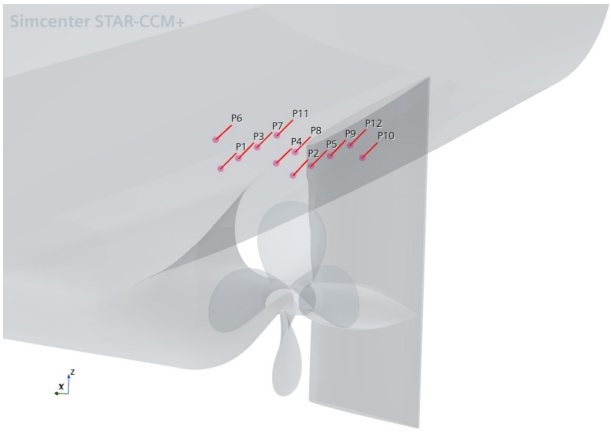

Figure 11: Location of the pressure probes shown from bottom view near the propeller

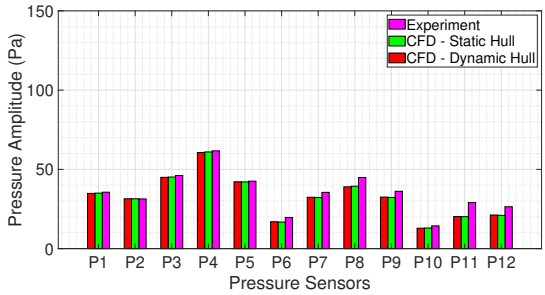

Figure 12: Pressure amplitudes at each probes for bollard pull case at 4.5rps

Furthermore, pressure recordings were investigated and compared with the experimental data using three turbulence models in the self-propulsion simulation (dynamic hull), with a forward speed of $U = 1.376$ m/s and a propeller rotational speed of $n = 7$ rps. Fig. 13 displays the pressure amplitudes for all 12 probes. In general, it is observed that the Elliptic Blending Reynolds Stress Model (EB-RSM) predicts results more closely aligned with the experimental data. RSM directly computes the Reynolds stress tensors and is capable of accounting for more complex interactions in turbulent flow fields. This capability may contribute to a more accurate estimation of pressure amplitudes using this model. The $SSTk-\omega$ turbulence model, on the other hand, exhibits less accuracy overall, except for probe-11. The FFT spectrum for the pressure at probe 4 is provided for all turbulence models and the experimental data in 14, as it exhibits the maximum pressure amplitude. It is evident that the Blade Passing Frequency (BPF) is consistently found to be around 28 Hz for all the turbulence models, matching the experimental data.

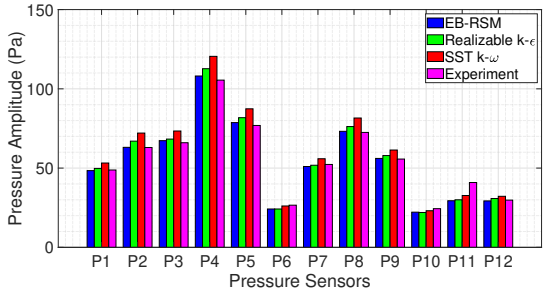

Figure 13: Pressure amplitudes at each probes for different turbulence modellings in self-propulsion case ($U = 1.376m/s$, $n = 7rps$)

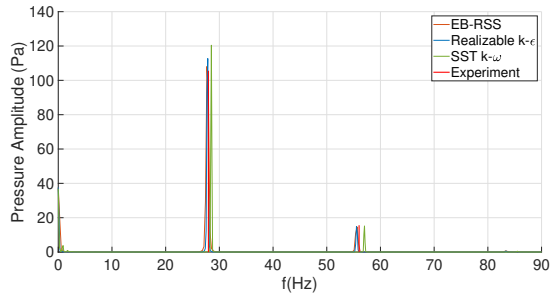

Figure 14: Fast Fourier Transform (FFT) of numerical pressure pulsations for probe-4

Finally, Table 8 compares the tow force at $n = 7rps$ for three turbulence models.

Table 8: Net tow force at $n = 7rps$ for different turbulence models

Turbulence Models	F (N)
Realizable $k-\epsilon$	5.690
$SSTk-\omega$	5.163
EB-RSM	6.587

4 CONCLUSION

In this study, RANS-based numerical simulations were carried out for a model-scale bulk carrier to predict its bare hull resistance curve, open-water propeller characteristics, and self-propulsion performance, validated against experimental data. It was observed that the global force results obtained from these simulations agree well with the experimental data.

Furthermore, pressure pulses in the behind-hull condition were also recorded and analyzed at 12 measurement probes for self-propulsion, using three RANS-based turbulence models: $SSTk-\omega$, Realizable $k-\epsilon$, and EB-RSM. It was found that EB-RSM predicts results better than the other models in comparison with the experimental data, while the $SSTk-\omega$ turbulence model exhibits the highest discrepancy.

Another simulation was conducted in a bollard pull condition, involving both static and dynamic hull scenarios, and the pressure amplitudes were compared with the experimental data. Probe-4, positioned directly above the propeller, recorded the highest pressure amplitude. In general, the pressure amplitudes closely matched the experimental data, except for probes 11 and 12, where the pressure amplitude was underpredicted. Furthermore, there was not much difference observed between the simulations performed with a static hull and those with a dynamic hull in terms of pressure amplitudes.

Future studies will focus on the numerical modeling of propeller-induced underwater noise under non-cavitating conditions.

ACKNOWLEDGMENTS

This work was supported by the Transport Canada through the "Propeller Induced Noise and Vibration (PINOV)" project.

REFERENCES

Gaggero, S., Tani, G., Villa, D., Viviani, M., Miglianti, F., Ausonio, P., Travi, P, Bizzarri, G., & Serra, F. (2017). 'Propeller geometry optimization for pressure pulses reduction: an analysis of the influence of the rake distribution' Fifth International Symposium on Marine Propulsors, Espoo, Finland.

Ge, M., Svennberg, U., & Bensow, R.E. (2019). 'Numerical Investigation of Pressure Pulse Predictions

for Propellers Mounted on an Inclined Shaft' Sixth International Symposium on Marine Propulsors, Rome, Italy.

Ge, M., Svennberg, U., & Bensow, R.E. (2020). 'Investigation on RANS prediction of propeller induced pressure pulses and sheet-tip cavitation interactions in behind hull condition' Ocean Engineering, 209.

Ge, M., Svennberg, U., & Bensow, R.E. (2021). 'Numerical Investigation of Propeller Induced Hull Pressure Pulses Using RANS and IDDES' Ninth International Conference on Computational Methods in Marine Engineering.

Jin, S., Peng, H., Qiu, W., Oldfield, C., & Stockdill, B. (2023). 'Best modeling practice for self-propulsion simulation of ship model in calm water' Physics of Fluids, 35.

Menter, F.R. (1994). 'Two-Equation Eddy-Viscosity Turbulence Models for Engineering Applications' AIAA Journal, Vol. 32, pp. 1598–1605.

Paik, K.J., Park, G.P., & Seo, J. (2013). 'URANS Simulations of Cavitation and Hull Pressure Fluctuation for Marine Propeller with Hull Interaction' Third International Symposium on Marine Propulsors, Tasmania, Australia.

Pallard, R. (2015).'Final report: tests to assess the effect of model construction on resistance' NRC Publications Archive.

'Practical Guidelines for Ship CFD Applications' ITTC.